Journal of Nuclear Materials 385 (2009) 563–571

Contents lists available at ScienceDirect

Journal of Nuclear Materials

journal homepage: www.elsevier.com/locate/jnucmat

Analysis of intergranular fission-gas bubble-size distributions in irradiated uranium–molybdenum alloy fuel ☆

J. Rest *, G.L. Hofman, Yeon Soo Kim

Argonne National Laboratory, 9700 S. Cass Avenue, Argonne, IL 60439, United States

ARTICLE INFO

Article history:
Received 15 October 2008
Accepted 3 January 2009

ABSTRACT

An analytical model for the nucleation and growth of intra and intergranular fission-gas bubbles is used to characterize fission-gas bubble development in low-enriched U–Mo alloy fuel irradiated in the advanced test reactor in Idaho as part of the Reduced Enrichment for Research and Test Reactor (RERTR) program. Fuel burnup was limited to less than ~7.8 at.% U in order to capture the fuel-swelling stage prior to irradiation-induced recrystallization. The model couples the calculation of the time evolution of the average intergranular bubble radius and number density to the calculation of the intergranular bubble-size distribution based on differential growth rate and sputtering coalescence processes. Recent results on TEM analysis of intragranular bubbles in U–Mo were used to set the irradiation-induced diffusivity and re-solution rate in the bubble-swelling model. Using these values, good agreement was obtained for intergranular bubble distribution compared against measured post-irradiation examination (PIE) data using grain-boundary diffusion enhancement factors of 15–125, depending on the Mo concentration. This range of enhancement factors is consistent with values obtained in the literature.

1. Introduction

Given the current uncertainties in materials properties, critical parameters, and proposed behavioral mechanisms, a key issue in modeling of fission-gas behavior in nuclear fuels is realistic validation. In general, the majority of model validation is accomplished by adjusting/predicting these properties and parameters to achieve agreement with measured gas release and swelling, and with mean values of the bubble-size distribution. However, the uncertainties in these properties and parameters generate an inherent uncertainty in the validity of the underlying physics and the physical reality of proposed behavioral mechanisms. This inherent uncertainty clouds the predictive aspects of any mechanistic approach to describing the phenomena. Thus, more detailed data is required in order to help clarify these issues.

The shape of the bubble-size distribution contains information on the nature of the behavioral mechanisms underlying the observed phenomena that are not present in the mean or average values of the distribution. This is due to information contained in the first and second derivates of the bubble density with respect to bubble size. Literature descriptions of measured intragranular bubble-size distributions [1] are few and far in between, and measured intergranular bubble distributions are all but non-existent. Here, we use measured intergranular bubble-size distributions [2] obtained from U–Mo alloy aluminum dispersion fuel developed as part of the RERTR program and irradiated in the Advanced Test Reactor (ATR) in Idaho.

An analytical model for the nucleation and growth of intra and intergranular fission-gas bubbles is described wherein the calculation of the time evolution of the average intergranular bubble radius and number density is used to set the boundary condition for the calculation of the intergranular bubble-size distribution based on differential growth rate and sputtering coalescence processes. Sputtering coalescence, or bubble coalescence without bubble motion, is a relatively new phenomena observed heretofore in implantation studies in pure metals [3]. In particular, the sputtering coalescence mechanism is validated based on the comparison of model calculations with the measured distributions. Recent results from TEM analysis of intragranular bubbles in U–Mo are used to validate the irradiation-induced diffusivity and re-solution rate used in the bubble-swelling model. Using these values, good agreement is obtained for intergranular bubble distribution compared against measured post-irradiation examination (PIE) data using grain-boundary diffusion enhancement factors of 15–125, depending on the Mo concentration. This range of enhancement factors is consistent with values obtained in the literature.

☆ The submitted manuscript has been authored by a contractor of the US Government under contract NO.DE-AC-02-06CH11357. Accordingly, the US government retains a non-exclusive royalty-free license to publish or reproduce the published form of this contribution, or allow others to do so, for US Government purposes. Work supported by US Department of Energy, Office of Global Threat Reduction, National Nuclear Security Administration (NNSA), under Contract DE-AC-02-06CH11357.

* Corresponding author. Tel.: +1 630 252 8065; fax: +1 630 252 5161.
E-mail address: jrest@anl.gov (J. Rest).

0022-3115/$ - see front matter © 2009 Elsevier B.V. All rights reserved.
doi:10.1016/j.jnucmat.2009.01.001

2. Experiment

Characteristic post-irradiation morphology of low-enriched U–Mo fuel cross sections are shown in Fig. 1 for several burnup levels. Fission-gas bubbles first appear on linear features, decorated heterogeneously over the fuel cross section (shown in Fig. 1(a)). The linear features are likely grain boundaries. There are virtually no visible bubbles in the interior of the grains. As burnup increases (~7.8–9.8% U), the bubble population increases on the grain boundaries and additional bubbles progressively spread to the interior regions (shown in Fig. 1(b)). At this stage, the fuel-swelling rate increases. The phenomenon underlying this increase in bubble nucleation and growth is grain refinement or 'recrystallization' of the gamma U-Mo. Eventually at higher burnup the entire fuel cross section is uniformly decorated with bubbles (shown in Fig. 1(c)).

The fuel particles used in the mini-plate tests were fabricated with the atomization process. A 'cellular' solidification structure is often found in rapidly cooled alloys that have a pronounced solidus–liquidus gap. An additional feature of the rapid solidification is a pronounced 'coring' within the grains. As a result, the center of the grains has a higher Mo content than the region surrounding the boundary. As shown in Fig. 2, the size and shape of the grains vary in the particle, frequently columnar in shape in the periphery whereas equiaxed and smaller in the interior.

Virtually all the grains at the periphery of C and D particles are columnar grains and A also has a few, as shown in Fig. 2(a). The columnar grains seem to have the same size regardless of the particle size. The particle A is larger than B, but B has larger grains in the interior part than A. This may be due to solidification and interdiffusion. The grain size measurement from the SEM picture in Fig. 2(b) is consistent with the measurement for grains from the as-fabricated plate. Comparison between the OM photo and SEM photo shows that the lines in the OM photo are grain boundaries in the SEM photo. The grain size distribution measured from the OM photo of Fig. 2(a) for V03 shows that, although there are some large grains observed, the predominant size is about 4 μm for this as-atomized fuel.

In order to obtain information on homogenous gamma U–Mo, some powder was annealed in the gamma phase prior to fuel plate fabrication. As a result of gamma-annealing, there are only large grains in Z03 and the cellular or subgrain structure has been eliminated (Fig. 3).

In Table 1 the irradiation conditions for the fuel plates used in the analysis are summarized.

All the results provided here are based on the measurements from SEM images of fracture surfaces. Because the fracture surfaces are not perfectly flat, bubble-containing features are not perfect lineal intercepts with the underlying grain boundaries. Also readings on SEM pictures with lower magnifications lead to uncertainties in the measurements. These experimental limitations may explain some of the variability in the measured bubble-size distributions. For some plates, different SEM pictures were available to obtain better counting statistics. The uncertainties related to the bubble-size measurements are ±10%, which leads to uncertainties ±20% in the spans between the maximum and minimum bubble sizes. The bubble-size populations for the middle bins are less affected by these uncertainties than those towards both ends. The errors for the middle bins are ±10% and for the end bins ±50%.

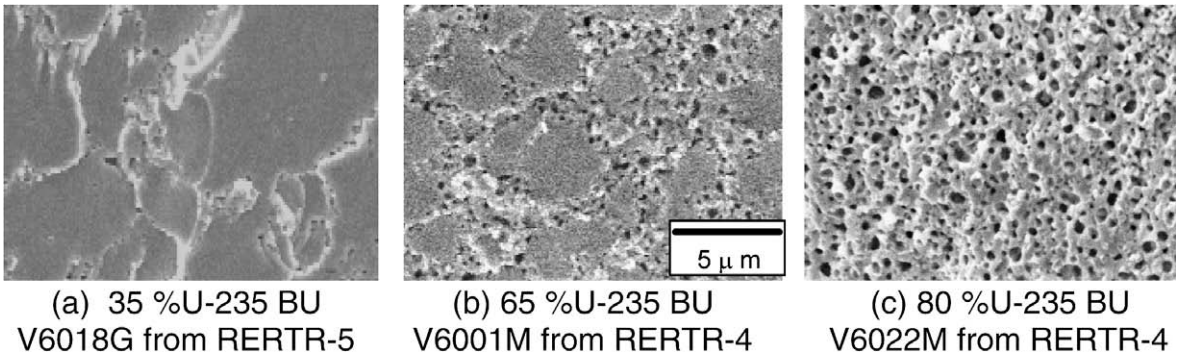

Fig. 1. SEM photos of irradiated U–Mo fuels from RERTR-4 and 5. The samples shown in this figure were fabricated with the same batch of atomized fuel particles and irradiated at similar temperatures.

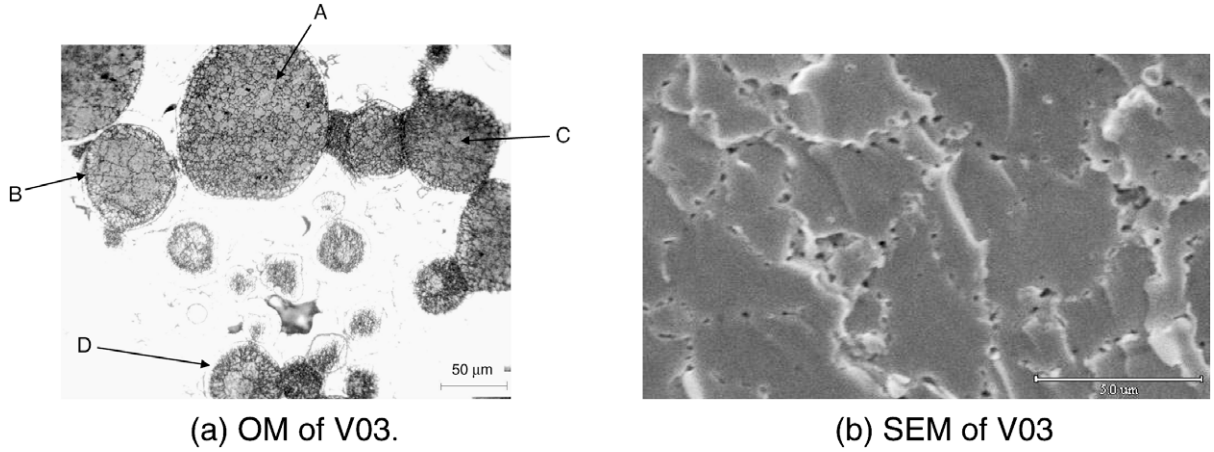

Fig. 2. OM (a) and SEM (b) of Mini-Plate V03.

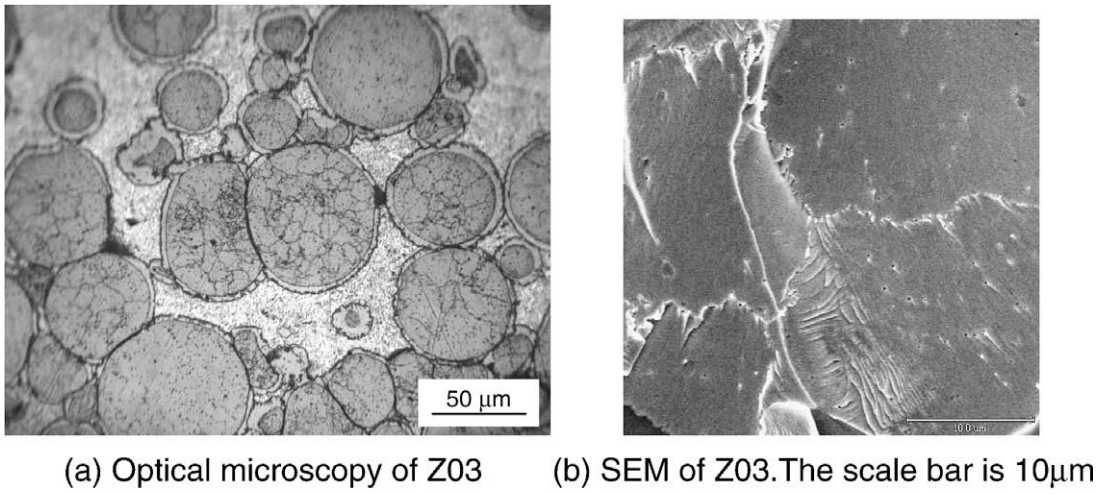

Fig. 3. OM and SEM micrographs of mini-plate Z03: fuel powder was gamma-phase annealed for 100 h at 800 °C before plate-fabrication.

Table 1
Description of fuel used in the analysis.

Test	Plate ID	Fuel property	Burnup (at.% U)	Fission rate (10^{14} f/cm^3 s)	Total duration (days)	Fission density (10^{21} f/cm^3)	Fuel Temp (°C)
RERTR-3	Z03	U–10Mo(a,g)	6.2	5.1	48	2.1	121
RERTR-3	Y01	U–10Mo(m,g)	5.8	4.8	48	2.0	109
RERTR-1	V002	U–10Mo(a)	7.6	3.2	94	2.6	66
RERTR-1	A003	U–10Mo(m)	7.8	3.3	94	2.7	68
RERTR-3	V07	U–10Mo(a)	5.8	4.8	48	2.0	122
RERTR-3	V03	U–10Mo(a)	7.4	6.0	48	2.5	149
RERTR-3	S03	U–6Mo(a)	7.6	6.8	48	2.8	158
RERTR-5	A6008H	U–10Mo(a)	9.6	3.3	116	3.3	177
RERTR-5	R6007F	U–7Mo(a)	7.2	2.6	116	2.6	185
RERTR-5	V6019G	U–10Mo(a)	9.6	3.3	116	3.3	142
RERTR-5	V6018G	U–10Mo(a)	6.8	2.3	116	2.3	121
RERTR-5	V8005B	U–10Mo(a)	7.2	2.5	116	2.5	170
RERTR-5	A8002L	U–10Mo(m)	9.4	3.2	116	3.2	191

a: Atomized, m: machined, g: annealed at 800 °C for 70–100 h.

The bubble size and number are measured on bubble-containing boundaries. For each SEM picture, the maximum and minimum bubble sizes were measured. The difference between the maximum and minimum was divided by seven. Therefore, for each fuel plate, seven size groups are used to characterize the bubble distribution.

Measured grain sizes for the plates used in the analysis are used to obtain bubble number density per unit fuel cross section area and subsequently number density per unit fuel volume. In order to obtain the bubble volume fraction, the bubble area fraction measured on the fuel cross section is needed. Because bubbles are homogeneously distributed, the bubble volume fraction is equal to the bubble area fraction measured on the cross section [4]. However, the SEM micrographs were taken on fuel fracture surfaces. Thus, the fuel grain is treated as a tetrakaidecahedron (TKDH) in order to convert the bubble density per unit length of grain boundary to bubble density per unit cross section area. The bubble area fraction can be obtained by using the average bubble size and bubble density per unit cross section area. Finally, in order to convert the data to bubble density per unit grain-boundary surface area, the bubbles on the grain surfaces of the TKDH are assumed to be uniformly distributed in a close-packed array. As a check, the bubble density on some exposed grain surfaces was measured directly. A comparison between the measured and the calculated data show good agreement [2].

3. Calculation of evolution of average intragranular bubble-size and density

The model presented here considers analytical solutions to coupled rate equations that describe the nucleation and growth of inter- and intragranular bubbles under the simultaneous effect of irradiation-induced gas–atom re-solution. The goal of the formulation is to avoid a coupled set of non-linear differential equations that can only be solved numerically, using instead a simplified, physically reasonable hypothesis that makes the analytical solutions viable. The gas-induced swelling rate is then assessed by calculating the evolution of the bubble population with burnup, and subsequently the amounts of gas in bubbles and lattice sites. Uncertain physical parameters of the model are determined by fitting the calculated bubble populations at given burnups with measured bubble size and density data.

At the irradiation temperatures of interest ($T < 500$ K), in analogy with UO_2, the diffusion of fission-gas atoms is assumed to be athermal with the gas–atom diffusivity D_g proportional to the fission rate $\dot{f}$. The gas–atom re-solution rate b is also assumed proportional to the fission rate.

Due to the strong effect of irradiation-induced gas–atom re-solution, in the absence of geometric contact, the bubbles stay in the nanometer size range. The density of bubbles increases rapidly early in the irradiation. At longer times, the increase in bubble concentration occurs at a much-reduced rate. Based on the above

considerations, a quasi steady-state solution for the average bubble density c_b and the average number of gas atoms per bubble m_b as a function of the density of gas in solution c_g and the gas atom radius r_g is given by [5]:

$$c_b = \frac{16\pi f_n r_g D_g c_g^2}{b m_b(t)}, \tag{1}$$

$$m_b(t) = \left(\frac{3b_v}{4\pi}\right)^{1/2}\left(\frac{4\pi D_g c_g(t)}{b}\right)^{3/2}. \tag{2}$$

In Eq. (1), f_n is the bubble nucleation factor, and in Eq. (2) b_v is the Van der Waals constant. In general, the value of f_n is less than one reflecting the premise that gas-bubble nucleation within the fuel matrix requires the presence of vacancies/vacancy clusters in order to become viable. The average bubble radius r_b is related to m_b through the gas law and the capillarity relation. Imposing gas–atom conservation, i.e., requiring that the sum of the gas in solution, in intragranular bubbles, and on the grain boundary is equal to the amount of gas generated (there is no gas released from the U–Mo fuel), the term $c_g(t)$ is determined as,

$$c_g(t) = \frac{-(1+f_s) + [(1+f_s)^2 + 64\pi f_n r_g D_g f \bullet \beta t/b]^{1/2}}{32\pi f_n r_g D_g/b}, \tag{3}$$

where β is the number of gas atoms produced per fission event and f_s is the fraction of gas released to the grain boundaries of grains of diameter d_g, where, following Speight [6]:

$$f_s \approx \frac{8}{d_g}\left(D_g\frac{b}{b+g}t\right)^{1/2} - \frac{6}{d_g^2}D_g\frac{b}{b+g}t, \tag{4}$$

where $g = 4\pi D_g r_b c_b$.

4. Calculation of evolution of average intergranular bubble-size and density

Following the work of Wood and Kear [7], grain-boundary bubble nuclei of radius R_b are produced until such time that a gas atom is more likely to be captured by an existing nucleus than to meet another gas atom and form a new nucleus. An approximate result for the grain-boundary bubble concentration is given by:

$$C_b = \left(\frac{8zaK}{12^{1/3}\pi^2\xi D_g\delta}\right)^{1/2}, \tag{5}$$

where a is the lattice constant, z is the number of sites explored per gas–atom jump, δ is the width of the boundary, ξ is a grain-boundary diffusion enhancement factor, and K is the flux of gas–atoms per unit area of grain boundary.

The intergranular bubble nucleation and growth formulation incorporated here is based on the assumption that, although the effect of radiation-induced re-solution on intergranular bubble behavior is not negligible, a reasonable approximation can be obtained by neglecting such effect in the governing equations [8]. Under the above considerations, the flux K of atoms at the grain boundary is given by:

$$K = f \bullet \beta\frac{d_g}{3}\frac{d(f_s t)}{dt}. \tag{6}$$

In general, in an irradiation environment where bubble nucleation, gas–atom diffusion to bubbles, and irradiation-induced re-solution are operative, a differential growth rate between bubbles of different size results in a peaked mono-modal size distribution [9]. The position of the peak in the bubble-size distribution that occurs under these conditions is defined by the balance between diffusion of gas–atoms to bubbles and irradiation-induced re-solution of atoms from bubbles. As more gas is added to the lattice (e.g., due to continued fission), the gas–atom diffusion flux to bubbles increases and the peak shifts to larger bubble sizes and decreases in amplitude, resulting in an increased level of bubble swelling with increased burnup. The model presented in this section describes the average behavior of this peak as a function of burnup.

5. Calculation of intergranular bubble-size distribution

Let $n(r)dr$ be the number of bubbles per unit volume on the grain boundaries with radii in the range r to $r+dr$. Growth by gas atom collection from fission-gas diffusing from the grain interior removes bubbles from this size range, but these are replaced by the simultaneous growth of smaller bubbles. The distribution of intragranular gas consists primarily of fission-gas atoms due to the strong effect of irradiation-induced gas–atom re-solution. Bubbles appear on the grain boundaries due to the reduced effect of re-solution, ascribed to the strong sink-like property of the boundary, as well as to the altered properties of bubble nucleation [8]. In addition, $n(r)dr$ is affected by bubble–bubble coalescence. A differential growth rate between bubbles of different size leads to a net rate of increase in the concentration of bubbles in the size range r to $r+dr$. This behavior is expressed by:

$$\left[\frac{dn(r)}{dt}\right]dr = -\frac{d}{dr}\left[n(r)\frac{dr}{dt}\right]_d dr - \frac{d}{dr}\left[n(r)\frac{dr}{dt}\right]_c dr, \tag{7}$$

where the subscripts d and c refer to growth by gas–atom diffusion and bubble coalescence, respectively. The growth rate (dr/dt) of a particular bubble is related to the rate (dm/dt) at which it absorbs gas from the boundary, either by diffusion of single gas atoms, or by coalescence with another bubble. The rate of growth due to gas–atom precipitation is controlled by the grain-boundary gas–atom diffusion coefficient ξD_g and the average concentration C_g of fission gas retained by the boundary.

Studies on the evolution of helium bubbles in aluminum during heavy-ion irradiation at room temperature have shown that bubble coarsening can take place by radiation-induced coalescence without bubble motion [3]. This coalescence is the result of the net displacement of Al atoms out of the volume between bubbles initially in close proximity. The resulting non-equilibrium-shaped bubble evolves toward a more energetically favorable spherical shape whose final size is determined by the equilibrium bubble pressure.

Bubble coalescence without bubble motion (sputtering coalescence) can be understood on the basis of a difference in the probability for an atom to be knocked out of the volume between a pair of bubbles and the probability of an atom to be injected into this inter-bubble volume. If the bubbles contained the same atoms as that comprising the inter-bubble volume, the net flux of atoms out of the inter-bubble volume would be zero. However, since the gas bubbles contain fission gas and not matrix atoms, the flux of atoms into the inter-bubble volume is reduced by the bubble volume fraction, i.e., the net flux out of the volume is proportional to $\lambda V - \lambda(V - V_B)$, where λ is the atom knock-on distance, and V_B is the intergranular bubble volume fraction. In this case, the growth rate (dr/dt) of a bubble being formed by the coalescence of two adjacent bubbles (and the commensurate effective shrinkage rate of the adjacent bubbles) is related to the rate (dm_s/dt) at which the inter-bubble material is being sputtered away, where

$$\frac{dm_s}{dt} = -b_s m_s. \tag{8}$$

Using the Van der Waals equation of state,

$$\frac{dr}{dt} = \frac{3(rkT + 2\gamma b_v)^2}{16\pi\gamma(kTr^3 + 3\gamma b_v r^2)}\frac{dm}{dt}. \tag{9}$$

Following the discussion above, the sputtering rate b_s can be expressed as:

$$b_s = \frac{6}{d_g}\lambda\delta_s f \bullet \pi r^2, \tag{10}$$

where the effective inter-bubble volume is assumed to be disk-shaped with volume = $\delta_s \pi r^2$, and where δ_s is the thickness of the material undergoing sputtering. For a lenticular bubble with radius of curvature ρ, the equivalent radius of a spherical bubble is given by:

$$r = \rho\left[1 - \frac{3}{2}\cos(\theta) + \frac{1}{2}\cos^2(\theta)\right]^{1/3}, \tag{11}$$

where

$$\cos(\theta) = \frac{\gamma_{gb}}{2\gamma}, \tag{12}$$

and γ_{gb} is the grain-boundary energy.

It is assumed that bubble coalescence is approached by the gradual erosion of the material between the bubbles. This bubble coarsening process can be visualized as lenticular intergranular bubbles separated by a distribution of solid discs. As these discs are sputtered due to fission damage, the majority of the sputtered atoms are injected into the adjacent bubbles, with the commensurate drawing together of the bubbles until the joining process has been completed. In order for this process to be viable, the gas atom knock-on distance should be sufficiently large such that the majority of atoms sputtered from the solid disc can enter the adjacent bubbles. Due to the geometry of the lenticular gas bubbles and solid discs, this distance will be substantially less than the inter-bubble spacing.

Inserting Eqs. (8)–(10) into the 2nd term on the right-hand side (rhs) of Eq. (7) and differentiating with respect to r,

$$\left(\frac{dn(r)}{dt}dr\right)_c = \frac{6}{d_g}\lambda\delta_s f \bullet \pi r^2 n(r)dr + \frac{2}{d_g}\lambda\delta_s f \bullet \pi r^3 \frac{dn(r)}{dr}dr. \tag{13}$$

Subsequent to intergranular bubble nucleation, gas arriving at the boundary will be adsorbed by the existing bubble population. The rate at which a grain-boundary bubble adsorbs gas is approximately given by:

$$dm/dt = 12\pi r \xi D_g C_g / d_g. \tag{14}$$

As mentioned in Section 4, re-solution of grain-boundary bubbles is not explicitly considered, e.g., in Eq. (14). The rationale for this is that due to the very strong sink-like nature of the grain boundary, gas–atoms ejected from a gas bubble located on the boundary that land within the steep portion of the concentration gradient are 'sucked back' into the boundary and quickly reenter the bubble such that the 'effective' re-solution rate is relatively small [8].

Combining Eqs. (9) and (14),

$$dr/dt = \frac{9r\xi D_g C_g (rkT + 2\gamma b_v)^2}{4\gamma d_g (kTr^3 + 3\gamma b_v r^2)} \approx \frac{3b_v \xi D_g C_g}{d_g r}. \tag{15}$$

Using the approximation on the right-hand side of Eq. (15), the first term on the rhs of Eq. (7) becomes,

$$\left(\frac{dn(r)}{dt}dr\right)_d = n(r)\frac{3b_v\xi D_g C_g}{d_g r^2} - \frac{3b_v\xi D_g C_g}{d_g r}\frac{dn(r)}{dr}. \tag{16}$$

The overall net rate of change of the concentration of bubbles in a given size range is given by the sum of Eq. (13) and Eq. (16),

$$\left(\frac{dn(r)}{dt}dr\right) = n(r)\frac{3b_v\xi D_g C_g}{d_g r^2} - \frac{3b_v\xi D_g C_g}{d_g r}\frac{dn(r)}{dr} - \frac{6}{d_g}\lambda\delta_s \times f \bullet \pi r^2 n(r)dr - \frac{2}{d_g}\lambda\delta_s f \bullet \pi r^3 \frac{dn(r)}{dr}dr. \tag{17}$$

The equilibrium population of bubbles is obtained by setting Eq. (17) to zero,

$$n(r)\frac{3b_v\xi D_g C_g}{d_g r^2} - \frac{3b_v\xi D_g C_g}{d_g r}\frac{dn(r)}{dr} - \frac{6}{d_g}\lambda\delta_s f \bullet \pi r^2 n(r)dr = 0, \tag{18}$$

where the last term in Eq. (17) has been omitted due to $\frac{3b_v\xi D_g C_g}{d_g r} \gg \frac{2}{d_g}\lambda\delta_s f \bullet \pi r^3$ for the conditions explored in this paper.

Eq. (18) must be solved subject to the relevant boundary condition. In general, this boundary condition concerns the rate at which bubbles are formed at their nucleation size r_0.

From a consideration of freshly nucleated bubbles [9],

$$n(r_0)dr = \left(\frac{C_b}{\tau_b}dr\right)\Big/(dr/dt)_{r=r_0}. \tag{19}$$

The rate of bubble nucleation is provided by the Wood–Kear nucleation mechanism [7] where on the grain boundary the average time τ_b for a gas atom to diffuse to an existing bubble (as discussed above this is the time at which bubble nucleation would essentially cease) is given by:

$$\tau_b = \frac{1}{\pi\xi D_g C_b}. \tag{20}$$

Thus, from Eq. (20) it follows that the bubble nucleation rate is given by:

$$\frac{dC_b}{dt} = \eta\frac{C_b}{\tau_b}, \tag{21}$$

where η is a proportionality constant that is determined by imposing the conservation of gas atoms.

The observed grain-boundary bubbles are a combination of lenticular-shaped objects whose size is substantially larger than the estimated thickness of the grain boundary [2]. In general, the solubility of gas on the grain boundary is substantially higher than in the bulk material. The gas concentration on the boundary will increase until the solubility limit is reached (approximately given by τ_b), whereupon the gas will precipitate into bubbles. Thus, the rate at which a grain-boundary bubble nucleus adsorbs gas is approximately given by:

$$(dm/dt)_{r=r_0} = b_v C_g/(4\tau_b C_b \pi r_0^3/3), \tag{22}$$

where C_g is given by:

$$C_g(t) = \frac{d_g}{3}f_s(t)c_g(t). \tag{23}$$

As described by Eq. (14), subsequent to bubble nucleation gas solubility on the boundary will drop to a relatively low value and gas arriving at the boundary will be adsorbed by the existing bubble population. Combining Eqs. (9), (22) and (23),

$$(dr/dt)_{r=r_0} = \frac{3C_g b_v (rkT + 2\gamma b_v)^2}{16\pi\gamma(4\tau_b C_b \pi r_0^3/3)(kTr^3 + 3\gamma b_v r^2)}. \tag{24}$$

The solution of Eq. (18) subject to the boundary condition expressed by Eqs. (19) and (24) is,

$$n(r) = \frac{64\eta\gamma C_b^2 \pi^2 r^3 (kTr^3 + 3\gamma b_v r^2)\exp[-\kappa(r^4 - r_0^4)]}{3b_v C_g d_g (rkT + 2\gamma b_v)^2}, \tag{25}$$

where

$$\kappa = \frac{\pi f \bullet \lambda\delta_s}{2b_v\xi D_g C_g}. \tag{26}$$

6. Comparison between model calculations and intragranular data

One of the major challenges in the field of fission-gas behavior in nuclear fuels is the quantification of critical materials properties.

Table 2
Values of parameters used in the calculations.

Parameter	Value	Reference
β	0.25	Olander [10]
ξ	15	(annealed) This work
	125	(non-annealed) This work
$b_0 (b = b_0 f \bullet)$	2×10^{-23} m^3	Spino/Rest [5]
$D_0 (D_g = D_0 f \bullet)$	10^{-39} m^3 s^{-1}	Matzke [15]
r_g	0.216 nm	Olander [10]
γ	0.5 J m^{-2}	(annealed) This work
	0.43 Jm^{-2}	(non-annealed) This work
$\cos(\theta)$	0.2	Hondros [16]
b_v	8.5×10^{-23} m^3/atom	Olander [10]
f_n	0.12	This work
δ_s	1×10^{-9} m	This work
λ	1.8×10^{-8} m	This work
Δ_0	2.5745×10^{-8} m	
Δ_i	1×10^{-9} m	

There is a direct correlation between the accuracy of the values of critical properties and the confidence level that the proposed underlying physics is realistic.

The values of the key parameters used in the model are given in Table 2. Many of them are known or estimated from the literature [10]; the values of the others (e.g., ξ) result from comparison of the present theory with measured data for bubble populations. As an example of estimated parameters, the values of D_g and b used for U–Mo are assumed to be the same as those for UO_2. Based on irradiation-enhanced creep rates measured in UO_2, UN and UC [11], the irradiation-enhanced gas–atom diffusivity D_g is expected to be lower in U–Mo than in UO_2. In addition, due to the higher thermal conductivity of the alloy as compared to the oxide, b is also expected to be lower in U–Mo than in UO_2. This argument is based on the expected larger interaction cross section in the metallic alloy with conduction electrons. However, because of the (assumed) linear dependence of both D_g and b on $f \bullet$, and because it is the ratio D_g/b that appears in Eqs. (1)–(3), it is reasonable to assume that this ratio of critical properties is the same for both materials.

The calculated intragranular bubble-size distribution compared with data [12] for the average bubble size and density in irradiated U–10 Mo fuel is shown in Table 3. Values for D_g and b obtained from data and analyses on UO_2 are listed in Table 2. The calculated results shown in Table 3 are in reasonable accord with the observed estimates of the average bubble density and size. However, it should be noted that the bubbles were observed to form a superlattice in the U–Mo with a relatively close spacing (6–7 nm) and having an approximate mono-modal like distribution [12].

Table 3
Intragranular results.

	Calculated	Data [12]
Bubble diameter (nm)	1.7	≈ 2
Bubble density (cm^{-3})	10^{19}	$\approx 3 \times 10^{18}$

7. Comparison between model calculations and intergranular data

The calculated distributions are obtained by integrating Eq. (25) over the bin sizes Δ_i, i.e., the bubble density $N(\Delta_i)$ in units of m^{-3} is,

$$N(\Delta_i) = \int_{\Delta_0+(i-1)\Delta}^{\Delta_0+i\Delta} n(r)\mathrm{d}r, \tag{27}$$

where Δ_0 is the minimum bubble size. The intergranular bubble size depends on the value of ξ (see Eq. (4) and Table 2), which is a grain-boundary gas–atom diffusion enhancement factor that reflects the fact that grain-boundary diffusion is decidedly faster than grain lattice diffusion [13,14]. The effect of ξ on the intergranular bubble nucleation is visible in Eq. (4). By increasing ξ the intergranular bubble density is reduced with a commensurate increase in bubble size. The larger value used for ξ for the non-annealed mini-plates reflects the increase in diffusivity with decreased molybdenum content.

Table 1 shows a description of fuel used in the analysis. This database consists of both as-atomized and gamma-annealed specimens. From Table 1, the range of burnup is from 5.8 to 9.2 at.% U, fission rate from 2.3 to 6.8×10^{14} f/cm^3 s, temperature from 66 to 191 °C, and Mo content from 6 to 10 wt%. Table 2 shows the value of the key physical parameters used in the model. As discussed in the previous section, many of these parameters are estimated based on their UO_2 values the remaining critical parameter ξ was determined by best overall interpretation of the measured intergranular bubble-size distributions for the gamma-annealed and for the as-atomized specimens, respectively.

Fig. 4 shows calculated results compared with RERTR-3 mini-plates Z03 and Y01 data. These mini-plates were fully annealed

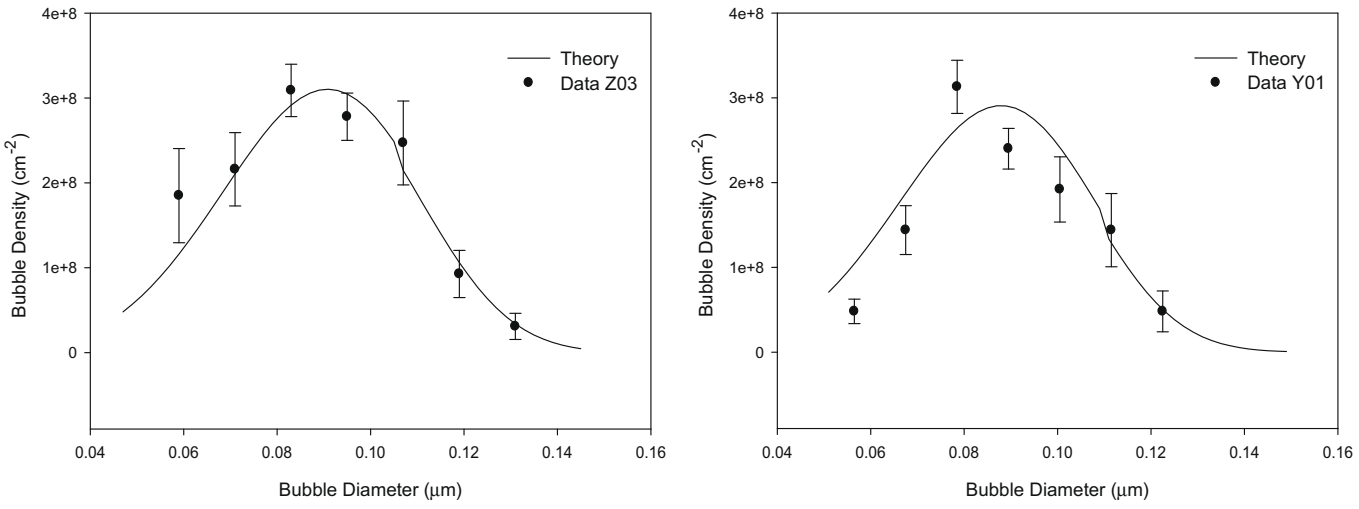

Fig. 4. Calculated and measured intergranular bubble-size distribution for U–10Mo gamma-annealed plates. Z03 was fabricated by atomization, whereas Y01 was made from ground powder.

and as such have a uniform distribution of molybdenum across the fuel region. Y01 was fabricated by atomization, whereas Y01 was made from a ground powder. The calculated distribution is in very good agreement with the measured quantities.

Fig. 5 shows calculated and measured intergranular bubble-size distribution for U–10Mo as-atomized plates. As is evident from the comparisons in Fig. 5, in general, the model calculations are in remarkable agreement with the data. Fig. 6 shows calculated and measured intergranular bubble-size distribution for U–6Mo, and U–7Mo as-atomized plates, respectively. The deviation between calculated and measured results shown in Fig. 6 is most likely due to the lower Mo content and, thus, requires different (larger) values for D_g and ξ.

The results of calculations shown in Fig. 7 demonstrate the increased validation leverage secured with the use of bubble-size distributions compared with the use of mean values (i.e., average

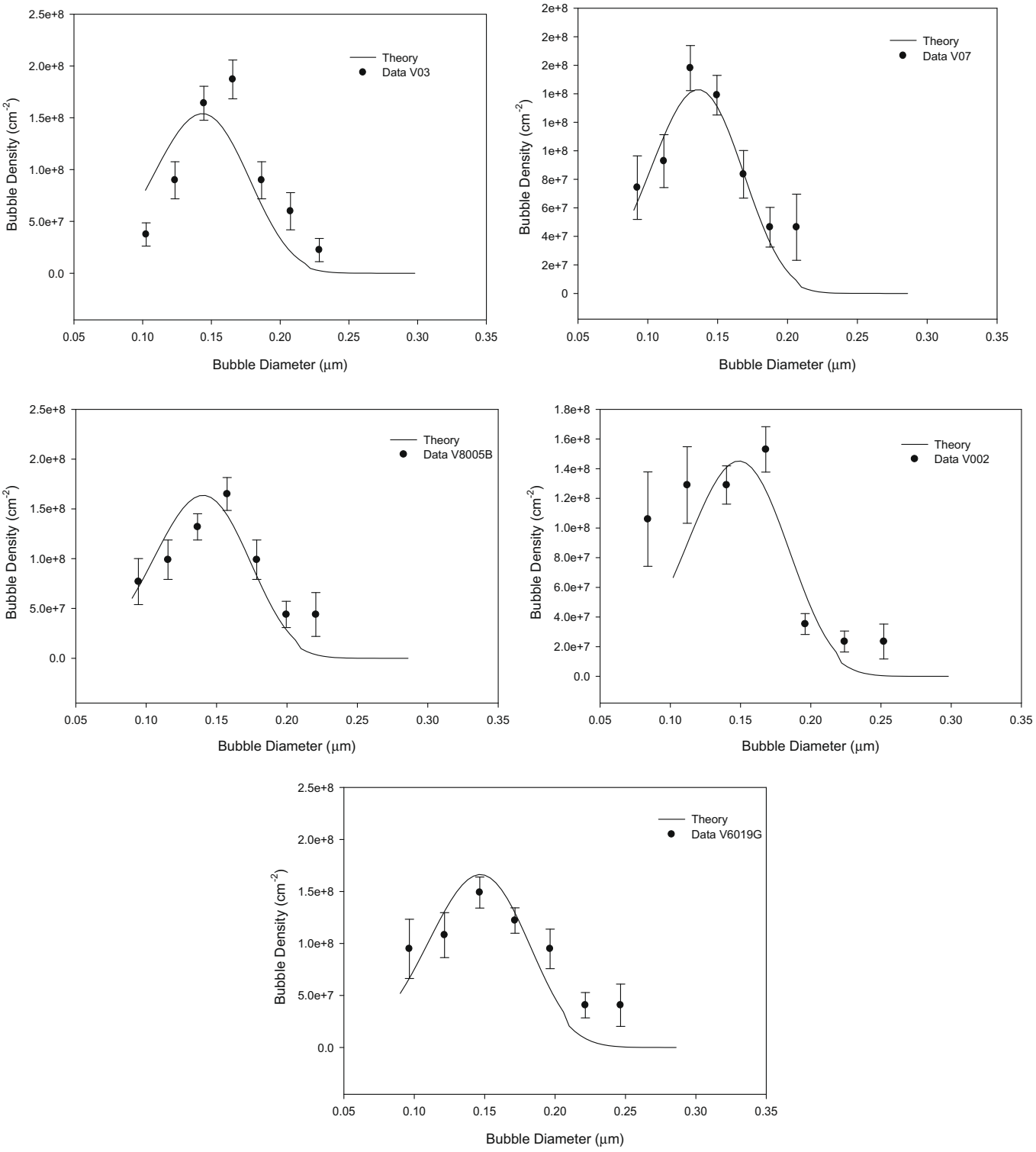

Fig. 5. Calculated and measured intergranular bubble-size distribution for U–10Mo as-atomized plates V03, V07, V002, V8005B, and V6019G.

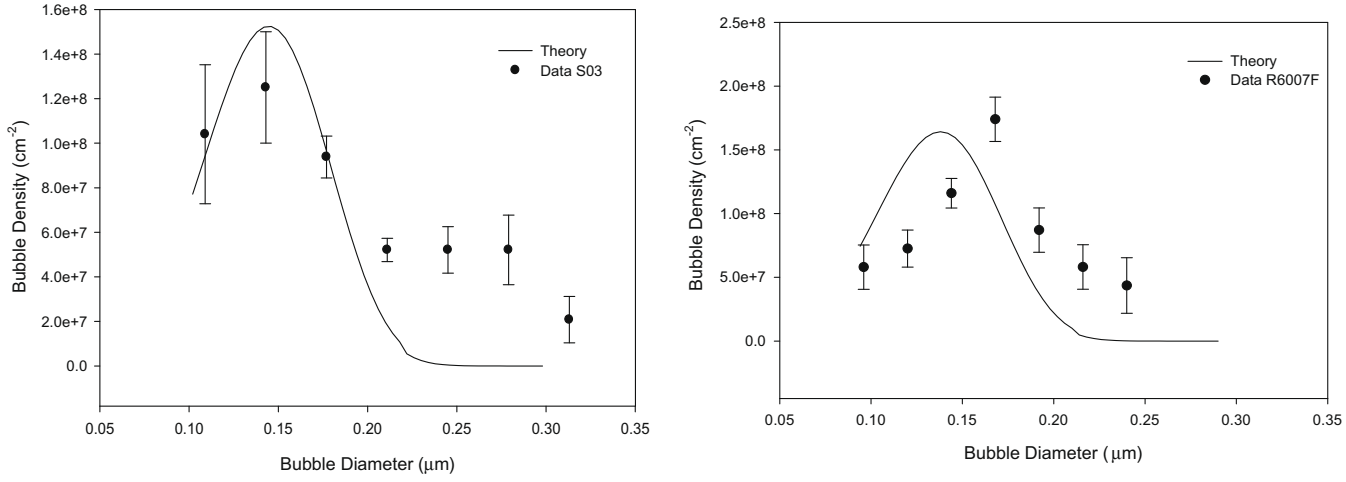

Fig. 6. Calculated and measured intergranular bubble-size distribution for as-atomized plates S03 (U–6Mo) and R6007F (U–7Mo).

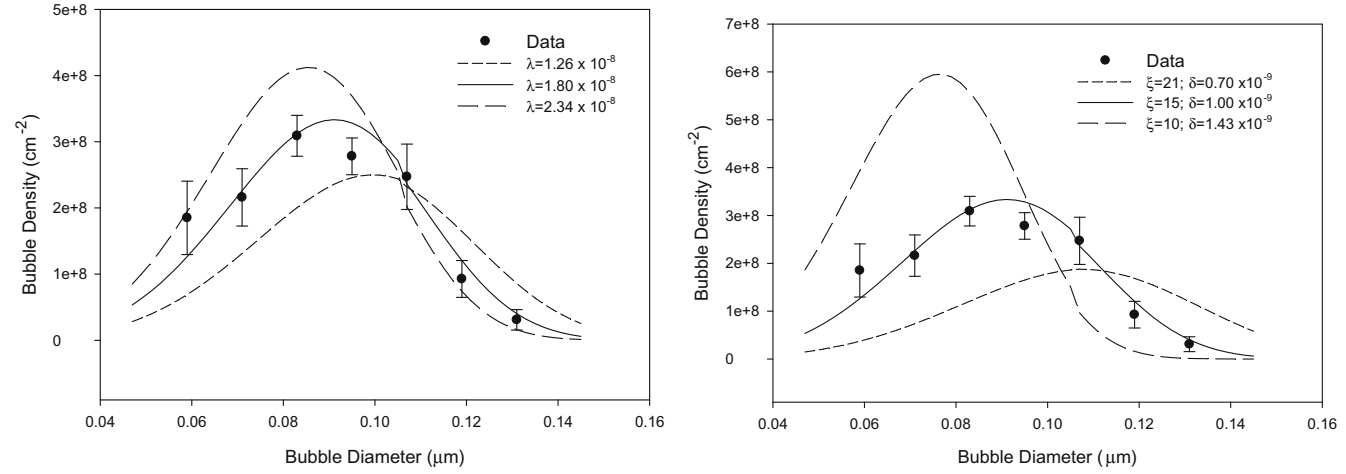

Fig. 7. Sensitivity of the calculated distributions to the value of the gas–atom knock-on distance (left hand graph). Results of a series of calculations made with paired values for the grain-boundary-diffusion enhancement factor and the thickness of the grain boundary, chosen such that the calculation of average quantities remains unchanged (right-hand graph).

quantities such as bubble density and diameter. Comparing model predictions with average quantities is by far the dominant validation technique reported in the literature). The graph on the left hand side of Fig. 7 shows the sensitivity of the calculated distributions to the value of the gas–atom knock-on distance. The right-hand graph in Fig. 7 shows the results of a series of calculations made with paired values for the grain-boundary-diffusion enhancement factor and the thickness of the grain boundary, chosen such that the calculation of average quantities remains unchanged. These calculated results demonstrate that the calculated distribution undergoes significant changes in shape as well as position and height of the peak. As such, the capacity to calculate bubble-size distributions along with the availability of measured distributions (as has been obtained from RERTR irradiated fuel plates) goes a long way in validating not only values of key materials properties and model parameters, but also proposed fuel behavioral mechanisms.

8. Conclusions

Calculations of intergranular bubble-size distribution made with a new mechanistic model for grain-boundary bubble formation kinetics are consistent with the measured distributions. Analytical solutions are obtained to the rate equations thus providing for increased transparency and ease of use. The results support a multi-atom gas-bubble nucleation mechanism on grain boundaries that have substantially higher gas solubility than that in the grain interior. The gas–atom diffusion enhancement factor on the grain boundaries was determined to be ~15–125 in order to obtain agreement with the measured distributions. The enhancement factor is about eight times higher for as-fabricated powder plates than for the annealed plates due to the lower Mo content on the boundaries. This range of values for the enhancement factor is consistent with values obtained in the literature [16]. The largest deviation between calculated and measured results (Fig. 6) is most likely due to several fuel plates that have a lower Mo content (6 and 7 wt% vs. 10 wt%) and, thus, require different (larger) values for D_g and ξ.

The agreement between the model and the measured distributions for the 10 wt% Mo fuel supports the validity of the proposed sputtering coalescence (bubble coalescence without bubble motion) coarsening mechanism on the grain boundaries. In this regard, attempts by one of the authors (J. Rest) to reproduce the shape of the intergranular bubble-size distribution using a model

based on the growth of bubbles in a regular array [17] have not been successful.

A number of the critical parameters listed in Table 2 are assumed to be the same as those listed in the literature for UO_2. However, it is the ratio of these parameters (b/D_g, ξ/λ) that appear in the model solution; thus, the validity of their use for U–Mo reduces to the ratios being approximately the same for both materials. This assumption is supported by the observed similarity (albeit remarkable) in bubble behavior and microstructure evolution between the two materials [18].

The results (e.g., see the RHS of Fig. 7) demonstrate the increased validation leverage secured with the use of bubble-size distributions compared with the use of mean values (i.e., average quantities such as bubble density and diameter). Model predictions are sensitive to various materials and model parameters. Improved prediction capability requires an accurate quantification of these critical materials properties and measurement data.

Acknowledgements

The authors would like to thank G.V. Shevlyakov (SSCR RIAR Dimitrovgrad, Ulyanovsk Region, Russia) for his assistance in measuring the bubble-size distributions.

References

[1] R.M. Cornell, Philos. Mag. 19 (1969) 539.
[2] Y.S. Kim, G.L. Hofman, J. Rest, G.V. Shevlyakov, Characterization of Intergranular Fission Gas Bubbles in U–Mo Fuel, Argonne National Laboratory Report, ANL-08/11, February, 2008.
[3] R.C. Birtcher, S.E. Donnelly, C. Templier, Phys. Rev. B 50 (1994) 764.
[4] R.T. DeHoff, F.N. Rhines, Quantitative Microscopy, McGraw-Hill Book Co., New York, 1968. p.45.
[5] J. Spino, J. Rest, W. Goll, C.T. Walker, J. Nucl. Mater. 346 (2005) 131.
[6] M.V. Speight, Nucl. Sci. Eng. 37 (1969) 180.
[7] M.H. Wood, K.L. Kear, J. Nucl. Mater. 118 (1983) 320.
[8] J. Rest, J. Nucl. Mater. 321 (2003) 305.
[9] M.V. Speight, J. Nucl. Mater. 38 (1971) 236.
[10] D.R. Olander, Fundamental Aspects of Nuclear Reactor Fuel Elements, Technical Information Center, ERDA, USA, 1976.
[11] M.R. Cundy, P. Von Der Hardt, R.H. Loelgen (Eds.), in: Measurement of Irradiation-Enhanced Creep in Nuclear Materials, J. Nucl. Mater. 65 (1977) 1–335.
[12] S. Van den Berghe, W. Van Renterghem, A. Leenaers, J. Nucl. Mater. 375 (2008) 340.
[13] N.A. Gjostein, in: Diffusion (Chapter 9), American Society for Metals, Metals Park, Ohio, 1973. p.272.
[14] J.C. Fisher, J. Appl. Phys. 22 (1951) 74.
[15] Hj. Matzke, Radiat. Eff. 53 (1980) 219.
[16] E.D. Hondros, in: K.C. Russell, H.I. Aaronson (Eds.), Precipitation Processes in Solids, The Metallurgical Society of AIME, 1976, p. 1.
[17] R.J. White, J. Nucl. Mater. 325 (2004) 61.
[18] G.L. Hofman, Y.S. Kim, Nucl. Eng. Tech. 37 (2005) 299.